The Journal of Chemical Physics

Quantum size effect affecting environment assisted electron capture in quantum confinements

Cite as: J. Chem. Phys. **150**, 224105 (2019); https://doi.org/10.1063/1.5095999
Submitted: 14 March 2019 . Accepted: 17 May 2019 . Published Online: 12 June 2019

Axel Molle, Essam R. Berikaa, Federico M. Pont, and Annika Bande

The Journal of Chemical Physics ARTICLE scitation.org/journal/jcp

Quantum size effect affecting environment assisted electron capture in quantum confinements

Cite as: J. Chem. Phys. 150, 224105 (2019); doi: 10.1063/1.5095999
Submitted: 14 March 2019 • Accepted: 17 May 2019 •
Published Online: 12 June 2019

Axel Molle,[1,2] Essam R. Berikaa,[1,3] Federico M. Pont,[4] and Annika Bande[1,a)]

AFFILIATIONS

[1] Department of Locally Sensitive and Time-Resolved Spectroscopy, Helmholtz-Zentrum Berlin für Materialien und Energie GmbH, Hahn-Meitner-Platz 1, 14109 Berlin, Germany
[2] Institute for Chemistry and Biochemistry, Freie Universität Berlin, Takustr. 3, 14195 Berlin, Germany
[3] Department of Nanotechnology Engineering, University of Science and Technology at Zewail City, Giza, Egypt
[4] Facultad de Matemática, Astronomía, Física y Computación, Universidad Nacional de Córdoba, and IFEG-CONICET, Ciudad Universitaria, X5000HUA Córdoba, Argentina

Note: This paper is part of a JCP Special Topic on Dynamics of Open Quantum Systems.
[a)] **Electronic mail:** annika.bande@helmholtz-berlin.de. **URL:** http://hz-b.de/theochem.

ABSTRACT

Ultrafast inter-Coulombic electron capture (ICEC) has been established as an important energy-transfer process in open paired-quantum-dot systems which can mediate between entrapment of free-moving electrons and release of trapped ones elsewhere by long-range electron-electron interaction within nanowires. Previous studies indicated ICEC enhancement through population and secondary decay of two-center resonance states, the latter known as inter-Coulombic decay (ICD). This study investigates the quantum-size effect of single- and double-electron states in an established model of a quasi-one-dimensional nanowire with two embedded confinement sites, represented by a pair of Gaussian wells. We analyze the ICEC related electron flux density as a function of confinement size and are able to clearly identify two distinct capture channels: a direct long-range electron-electron impulse and a conversion of kinetic energy to electron-electron correlation energy with consecutive ICD. The overlay of both channels makes ICEC extremely likely, while nanowires are a strong candidate for the next miniaturization step of integrated-circuit components.

I. INTRODUCTION

Size is a key factor in the electronic industry. While screens get bigger, electronic circuits become gradually smaller. Quantum effects arise which offer challenges and interesting new possibilities. Semiconductor technology has already grown and shaped electronics exponentially in the 1960s such that integrated circuits doubled the number of hosted transistors annually.[1] Known as Moore's Law, this quest for exponential reduction in electronic component size had already just reached the nanometer scale with commercial transistors of 800 nm size in 1989[2–4] and has continued to fuel technological development and progress. Having reached 45 nm size in 2007,[5] current mass-produced transistors for mobile-phone processors use etched narrow fin-shaped structures approaching 7 nm thickness,[6–8] which is only three times the size of human DNA. Although the reduced size is pursued to achieve lower form factors of electronic products and higher component density on the individual integrated circuit, it offers significant technological challenges as nanometer-sized electronics leave the regime of classical physics and become governed by quantum-mechanical effects.[9] The dominating electronic components remain the same four basic elements of resistor, capacitor (light-emitting), diode, and transistor, but 100×10^6 of them are assembled on less than 1 cm^2.[10]

Known as the quantum size effect,[11–13] the quasicontinuous band structure of any bulk material splits up into discrete energy

levels when its size is reduced sufficiently.[14,15] Similarly, regions of crystal defects, impurities, or atoms in contrast to their surrounding material can change optical and electrical properties by inducing quantum effects. Therefore, nanostructured electronic components which are essentially open quantum systems play a vital role in fostering a wealth of applications: from lasers[16] to solar cells,[17] from data storage[18] to displays,[19] and from their application as sensors[20] to their potential as qbits.[21]

To further miniaturize technology to yet unachieved component density, nanowires prove to be strong candidates to reach the next research-and-development target—the so-called *5-nm node*.[22–24] We therefore investigate the confinement-size dependent capture of a free-moving electron through long-range interaction with another nearby electron confined in the vicinity as might be encountered in a device built from two quantum dots, A and B, within a nanowire.[25–28] This process has been discussed as "environment-assisted electron capture" and as "inter-Coulombic electron capture" (ICEC). It was predicted with electron dynamics for pairs of quantum dots[29–31] as well as with scattering theory for pairs of atoms and molecules where it had been called inter*atomic* Coulombic electron capture originally.[32,33] Most recently, *ab initio* R-matrix computations demonstrated the importance of ICEC for Ne^+ in He droplets.[34] Within ICEC, an electron in an initially charged confinement B^- feels a momentum pressure through long-range Coulomb repulsion from a moving electron penetrating a neighboring confinement A. As the incident electron transfers energy to its distanced partner, it is captured into A and forces the neighboring electron to leave its respective confinement according to

$$e^-_{in} + A{+}B^- \longrightarrow A^-{+}B + e^-_{out}. \tag{1}$$

While the choice of material composition and doping offers essential control over electronic device performance, it remains limited by availability, material cost, and technical feasibility. Tuning the electron confinement size and thereby exploiting the quantum size effect, however, offers an alternative which is easily portable to industrial scale. This study therefore investigates how size affects efficiency and selectivity of ICEC. Electron dynamics of ICEC in quantum dots confirmed an energy-selective reaction pathway through decay of a macroscopic two-center resonance state $(AB)^*$ known by itself as *inter-Coulombic decay* (ICD), following

$$e^-_{in} + A{+}B^- \xrightarrow{\text{ICEC}} (A^-{+}B^-)^* \xrightarrow{\text{ICD}} A^-{+}B + e^-_{out}. \tag{2}$$

Like inter-Coulombic electron capture, inter-Coulombic decay is mediated through long-range Coulomb interaction of electrons located on two different partner sites, may it be atoms and molecules where it was originally called inter*atomic* Coulombic decay[35–37] or solid state confinements as quantum dots.[38–40] Here, an electron in the excited state of reaction partner A^{-*} relaxes to a lower energy state as its excess energy becomes available for ionization of the other partner B^-. Compared to the young prediction of ICEC, however, inter-Coulombic decay is already well established in various fields, such as helium droplets,[41] hollow atoms,[42] as well as biological systems,[43,44] and nanostructures as fullerenes[45] or quantum films.[46,47] Different ways to achieve ICD resonance have been studied, namely, by radiation[37] or impact of ions,[48,49] α-particles,[44] and ultimately electrons,[29,32,50] the pathway we are discussing hereafter.

The full electron dynamics of the ICEC process is going to be calculated in a charged quantum-dot-pair model of two Gaussian binding potentials.[29–31] In this comparably small system, it is possible to solve the time-dependent Schrödinger equation at a high level of numerical accuracy regarding electron-electron correlation by using the multiconfigurational time-dependent Hartree (MCTDH) approach[51,52] with fermionic antisymmetrization of a discrete-variable-represented (DVR) wavefunction as implemented in the Heidelberg software suite.[53,54] This gridlike approach bears the merit of offering access to the full electron dynamics while treating continuum states on the same footing as bound ones which is not usually achieved with many other theoretical methods.

While it was previously shown that ICD can enhance the overall ICEC probability in comparison with a direct ICEC without ICD,[29–31] we show in this study that the two reaction pathways are distinct in their energy signature, a broadband energy transfer echoing the incoming electron in the case of direct ICEC against energy selection through resonance criteria of ICD. As a consequence of the quantum-size effect, ICD and ICEC must depend on the size of the electronic confinements which has been investigated in the case of ICD.[55,56] Here, we intend to use the effect to study the particular interplay between ICD and ICEC, whereas a following empirical high-throughput study on ICEC in quantum dots will disentangle the particular dependence of maximal ICEC probability density on eigenenergy interrelations.[57] The primary interest in the present study is the electron flux associated with a successful inter-Coulombic electron capture in a nanowire-embedded pair of quantum dots at different confinement sizes and constant initial states. Though theoretical in nature, our investigation mimics the experimentally known and easiest access to energy-level variation of quantum dots via the well known quantum-size effect.

In order to analyze the individual contributions of the inter-Coulombic electron capture channels, we describe the general evolution and kinetics of free-moving Gaussian wavepackets in Sec. II A and generic decaying quantum states in Sec. II B, before introducing the paired-quantum-dot model (Sec. II C) and deducing expectations toward ICEC dynamics of individual reaction channels and their distinguishability in the electron flux density (Sec. II D). Related computational details are comprised in Sec. III. To dissect the size dependence of ICEC, we start the discussion of numerical results by characterizing the traditional quantum-size effect of monoelectronic and dielectronic eigenenergies to which there has not been any analytical solution found (Sec. IV A). Consequently, we explain an example of the evaluation of the undertaken dynamics calculation in Sec. IV B before eventually concentrating on the size dependence of the individual reaction pathways of ICEC.

II. THEORETICAL BACKGROUND

A. Free wavepackets

A free particle moving through a medium can be described by a Gaussian wavepacket of initial average position Z, initial group

velocity p_0/m^*, and initial uncertainty in position σ_z. At this point, we wish to consider one spatial dimension only which is to be denoted by z and reads

$$\langle z, t_0|\phi\rangle := \left(\frac{1}{2\pi\sigma_z^2}\right)^{\frac{1}{4}} \exp\left[-\frac{1}{4}\left(\frac{z-Z}{\sigma_z}\right)^2 + \frac{i}{\hbar}p_0(z-Z)\right]. \quad (3)$$

Although the expected position of the particle is determined up to some uncertainty at initial time t_0, it becomes less certain where it may be found as time evolves or where it would have been found at a preceding point in time. In other words, the wavepacket at t_0 has minimum uncertainty, while more generally speaking, uncertainty $\sigma_z(t)$ and average position $Z(t)$ of the wavepacket depend on time according to

$$\sigma_z^2(t) = \sigma_z^2(t_0) + \frac{i\hbar}{2m^*}(t-t_0), \quad (4)$$

$$Z(t) = Z(t_0) + \frac{p_0}{m^*}(t-t_0). \quad (5)$$

Furthermore, we can deduce the initial distribution in momentum space by the Fourier transformation of Eq. (3),

$$\langle p, t_0|\phi\rangle = \left(\frac{2\sigma_z^2}{\pi\hbar^2}\right)^{\frac{1}{4}} \exp\left[-\left(\frac{\sigma_z}{\hbar}\right)^2(p-p_0)^2 + \frac{i}{\hbar}Z(p-p_0)\right]. \quad (6)$$

By expressing the momentum in terms of energy ε as $p = -\sqrt{2m^*\varepsilon}$ for $p \le 0$ and $p = \sqrt{2m^*\varepsilon}$ for $p > 0$ in the normalization integral, $1 = \int_{-\infty}^{\infty} dp\left|\langle p, t_0|\phi\rangle\right|^2$, and then identifying the integrand as the particle's initial energy distribution by $D_\phi(\varepsilon)$, we find

$$D_\phi(\varepsilon) = \left(\frac{m^*\sigma_z^2}{\pi\hbar^2}\right)^{\frac{1}{2}}(\varepsilon)^{-\frac{1}{2}}\left(\exp\left[-2\left(\frac{\sigma_z}{\hbar}\right)^2\left(\sqrt{2m^*\varepsilon} - p_0\right)^2\right] + \exp\left[-2\left(\frac{\sigma_z}{\hbar}\right)^2\left(\sqrt{2m^*\varepsilon} + p_0\right)^2\right]\right). \quad (7)$$

B. Decaying states

In contrast to the state $|\phi\rangle$ of a free wavepacket, one can also consider an arbitrary metastable quantum state $|\mu\rangle$ of some sort which is to be characterized by a decay in time $t > t_0$ with decay rate $\Gamma/(2\hbar)$, energy expectation value E_μ, and initial space-time-dependent amplitude $\langle z, t_0|\mu\rangle$ and reads

$$\langle z, t \ge t_0|\mu\rangle := \exp\left[-\frac{\Gamma}{2\hbar}(t-t_0) - \frac{i}{\hbar}E_\mu(t-t_0)\right]\langle z, t_0|\mu\rangle. \quad (8)$$

By Fourier transforming this equation, we can express the decaying state in terms of the complex Siegert energy $E_\mu - i\frac{\Gamma}{2}$ as quantum amplitude of energy E,

$$\langle z, E|\mu\rangle = \left(\frac{\hbar\Gamma}{4\pi}\right)^{\frac{1}{2}} \frac{i\langle z, E_\mu|\mu\rangle}{E - \left(E_\mu - i\frac{\Gamma}{2}\right)}, \quad (9)$$

at the spatial position z with respect to the reference amplitude $\langle z, E_\mu|\mu\rangle$ at energy expectation value E_μ.

It is well-known and apparent that the energy distribution $D_\mu(E)$ of such a metastable state is given by the Cauchy-distribution probability-density function

$$D_\mu(E) = \left(\frac{\hbar}{\pi\Gamma}\right)\frac{\Gamma^2}{\Gamma^2 + 4(E-E_\mu)^2}, \quad (10)$$

often referred to as the Lorentzian function or Breit-Wigner distribution of the resonance energy E_μ and the full-width at half-maximum Γ.[58]

C. Model system

We consider charge carriers moving along a nanowire with an embedded pair of quantum dots. This provides an example of a quasi-one-dimensional open quantum system,[23,29] where electrons can enter, pass through, and leave the medium. It allows a treatment of reduced dimensionality as carrier transport through the wire is predominantly bound to one spatial dimension.

Solid state physics generally accounts for collisions of moving charge carriers with the medium's crystal structure and other related resistant effects. This is done by assigning a material-dependent effective mass m^* to the charge carrier. By this so-called "effective mass approximation," the carrier in the medium may then be treated analogously to a particle in free space as discussed in Sec. II A. Although the effective mass is dependent on material and other experimental conditions, the mathematical treatment becomes independent from the medium described. Consequently, it is possible to define effective units in analogy with the free-space entities. "Atomic units" define the fundamental quanta of electron mass m_e, elementary charge e, action $\hbar$, and Coulomb force constant $(4\pi\varepsilon_0)^{-1}$ as respective units of reference, that is, [1 a.u.] each. In dependence on the material, one can thus define an effective Bohr radius,[59]

$$a_B^* = \frac{4\pi\varepsilon\hbar^2}{m^*e^2}, \quad (11)$$

as the length of reference as well as an effective energy $E_H^* = \frac{\hbar^2}{(m^*a_B^{*2})}$ as reference energy analogously to the Hartree energy[59,60] and, accordingly, time scales in units of $\hbar/E_H^*$ and momentum in units of $\hbar/a_0$. This takes material-dependent quantities such as dielectric permittivity ε and effective carrier mass m^* into account. Note that the reference scale for electric charge could similarly be adapted to the particular charge carrier considered but shall remain the elementary charge e for the purpose of this study.

In such an effective-mass description, a local change in material or local defect in crystal structure may trap the charge beyond the statistical average. This can be described by an appropriate binding potential. The embedding of a material within another medium is thereby often modeled by a finite square box potential. Nevertheless, a different choice of potential might also account for effects like Schottky barriers,[61] energy band bending in junctions of n- and p-doped materials,[62,63] atom diffusion and wetting layer effects,[64] Fermi level unpinning,[24,65] or tilted potentials inducing charge separations as found in superlattices of zinc-blendes and wurtzites.[66,67]

The nanostructure we intend to consider in this study thus consists of a virtually infinite semiconducting wire with two embedded regions of confinement at center-to-center distance $\mathscr{R}$. Assuming injected electrons as charge carriers to be described, one might talk of a p-type host material in junction with two n-type regions in the form of a pair of PNP heterojunctions. We denote the longitudinal transport direction of the wire as z and distinguish the quantum dots as the "left" or "right" one of respective confinement length $\mathscr{L}_L$ or $\mathscr{L}_R$ and band steps $V_{L/R}$ with respect to the surrounding wire. The smooth potential V_{QD} for this quantum-dot pair can then be modeled by the following equation which describes a pair of Gaussian wells shown as a blue line in the bottom of Fig. 1:[38]

$$V_{QD}(z) := -D_L \exp\left[-2\left(\frac{z+\frac{\mathscr{R}}{2}}{\mathscr{L}_L}\right)^2\right] - D_R \exp\left[-2\left(\frac{z-\frac{\mathscr{R}}{2}}{\mathscr{L}_R}\right)^2\right]. \quad (12)$$

We define the single-electron Hamiltonian $\hat{h}$ of longitudinal kinetic energy and quantum-dot potential operator $V_{QD}(z)$ as

$$\hat{h} := -\frac{\hbar^2}{2m^*}\frac{\partial^2}{\partial z^2} + V_{QD}(z). \quad (13)$$

It gives rise to a set of eigenenergies $\{E_n\}_n$ and associated eigenstates $\{|n\rangle\}_n$ according to

$$\hat{h}\,|n\rangle =: E_n\,|n\rangle \quad \forall n. \quad (14)$$

For simplicity, we restrict our system to cases of a single bound state $|R\rangle$ of the right quantum dot, as well as a ground and a single excited state of the left quantum dot, $|L_0\rangle$ and $|L_1\rangle$, respectively. As localization should be distinguishable in appropriately separated quantum dots, we choose to label single-electron bound eigenstates according to their position. Unbound eigenstates are named by their free energy ε within the continuum, i.e.,

$$\{|n\rangle\}_n =: \left\{|L_0\rangle, |R\rangle, |L_1\rangle, \{|\varepsilon\rangle\}_{\varepsilon\geq 0}\right\}. \quad (15)$$

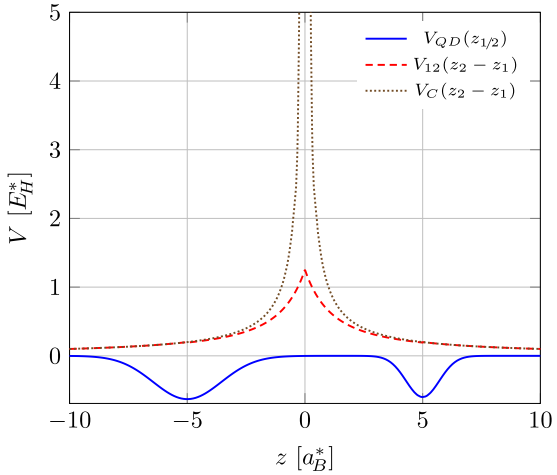

FIG. 1. The binding potential V_{QD} (blue solid line) modeling the quantum dot pair as a function of z is shown in conjunction with the true Coulomb potential V_C (brown dotted line) and the effective Coulomb potential V_{12} (red dashed line) as a function of spatial distance $z = |z_2 - z_1|$ between the electrons.

Assuming a longitudinal setup of the charge carrying medium in the form of a wire and neglecting direct ionization out of the wire, the charge carriers are transversally bound. This means the nanowire acts as a waveguide of transversal oscillator strength $\hbar\omega_\perp$ to the particles moving through it. This has successfully been described by the harmonic potential $U_\perp$ and associated transversal ground state $|0\rangle_\perp$,[68] where a natural length l is associated to the product of oscillator strength $\hbar\omega_\perp$ and material-dependent effective mass m^* according to the equations

$$U_\perp(x,y) := \hbar\omega_\perp\left(\frac{x^2+y^2}{2l^2}\right), \quad (16)$$

$$\langle x,y|0\rangle_\perp := \left(\pi l^2\right)^{-\frac{1}{4}} \exp\left[-\frac{x^2+y^2}{2l^2}\right], \quad (17)$$

$$l := \sqrt{\frac{\hbar}{m^*\omega_\perp}}. \quad (18)$$

Generally, the Coulomb repulsion between two electrons is dependent on the distance between them with the usual $1/r$ dependence. The repulsion strength is medium dependent. The Coulomb potential $V_C(\vec{r}_1, \vec{r}_2)$ in three spatial dimensions can therefore be expressed in terms of the aforementioned effective medium-incorporated units of natural scales of energy E_H^* and length a_B^* as

$$V_C(\vec{r}_1, \vec{r}_2) = E_H^* \frac{a_B^*}{|\vec{r}_2 - \vec{r}_1|}. \quad (19)$$

We assume energies small enough to keep electrons transversally in their spatial ground-state distribution, i.e., $E \overset{!}{<} 3/2\,\hbar\omega_\perp$, while they travel longitudinally through the wire. Under this assumption, one can average over the transversal contributions to the full-dimensional Coulomb potential of interaction between a transversal electron-distribution according to Eq. (17) at longitudinal position z_1 and another one at z_2. This reduces the problem under investigation to a quasi-one-dimensional open quantum system with effective interaction potential

$$V_{12}(z_1, z_2) = E_H^* \frac{a_B^*}{l}\sqrt{\frac{\pi}{2}}\, w\left(i\frac{|z_2 - z_1|}{\sqrt{2}l}\right) \quad (20)$$

$$\text{with } w(iz) := \left(1 - \operatorname{erf}[z]\right) \exp\left[z^2\right] \quad (21)$$

and has been employed successfully.[29,31,40] Note here that $w(iz)$ is the Faddeeva function,[69] and the effective potential V_{12} thus exhibits a shape related to the Voigt profile (dashed line in Fig. 1)[69] compared to the diverging profile of the true Coulomb interaction $V_C(\vec{r}_1, \vec{r}_2)$ displayed for $x_{1/2} = y_{1/2} = 0$ (Fig. 1, dotted line).

Due to the fermionic nature of the two electrons investigated here, their total wavefunction has to obey Pauli's exclusion principle. The wavefunction describing an electron in an arbitrary state $|\alpha\rangle$ and another in an arbitrary state $|\beta\rangle$ shall hence be given by their antisymmetric outer product and denoted by $|\alpha\beta\rangle$,

$$|\alpha\beta\rangle := \frac{1}{\sqrt{2}}\left(|\alpha\rangle\otimes|\beta\rangle - |\beta\rangle\otimes|\alpha\rangle\right). \quad (22)$$

Accordingly, a projection of the overall wavefunction onto the two-electron state $|\alpha\beta\rangle$ is defined by the outer product of a state with itself and is being denoted

$$\hat{\mathbb{P}}_{\alpha\beta} := |\alpha\beta\rangle\langle\alpha\beta|. \tag{23}$$

Furthermore, we wish to consider a projection $\hat{\mathbb{P}}_\alpha$ of the two-electron wavefunction on an arbitrary single-electron state $|\alpha\rangle$, which describes the wavefunction of one electron coinciding with another one occupying state $|\alpha\rangle$. Such a projector is mathematically described by the symmetric outer product of state $|\alpha\rangle$ with the identity operator $\mathbb{1}$ as

$$\hat{\mathbb{P}}_\alpha = \tfrac{1}{2}\big(|\alpha\rangle\langle\alpha|\otimes\mathbb{1} + \mathbb{1}\otimes|\alpha\rangle\langle\alpha|\big). \tag{24}$$

We wish to numerically undertake an ICEC experiment. For that purpose, we charge the right quantum confinement and send a free electron toward the paired quantum confinement from the left. That means we prepare an electron in bound state $|R\rangle$ and another in free state $|\phi\rangle$ according to Eq. (3) at a large distance from the quantum-confinement region. We then antisymmetrize according to Eq. (22) to reach the total state $|\Psi\rangle$. In general, $|\Psi\rangle$ is not separable into single-electron components due to electron-electron interaction. At an infinite distance, however, the electrons cannot interact and are effectively independent from each other. This implies the two-electron wavefunction $\langle z_1, z_2|\Psi\rangle$ can be well approximated by antisymmetrically combined single-electronic components within the large-distance limit as

$$|\Psi_0\rangle := |\phi R\rangle = \tfrac{1}{\sqrt{2}}\big(|\phi\rangle\otimes|R\rangle - |R\rangle\otimes|\phi\rangle\big). \tag{25}$$

As we wish to consider two-electron states from here on, we use index "1" or "2" to indicate single-electron quantities where appropriate. The Hamilton operator $\hat{h}_1$, for example, shall refer to the operator sum of quantum-confinement potential V_{QD} and kinetic energy operator as introduced in Eqs. (12) and (13) which act on the electron labeled "1." Furthermore, the electronic interaction potential V_{12} is contained. We thereby arrive at the system's Hamilton operator

$$\hat{H} = \hat{h}_1 + \hat{h}_2 + V_{12}. \tag{26}$$

D. ICEC dynamics

Analyzing the evolving state $|\Psi\rangle$ at large times, we can assure that an inter-Coulombic electron capture has taken place if we observe an electronic current at a large distance from the confinement region coinciding with some occupation of the left-bound single-electron states $|L_0\rangle$ and $|L_1\rangle$. We therefore define the flux operator $\hat{F}$ such that its expectation value $F(t)$ as a function of time describes the electron flux at longitudinal position z_F. Similarly, $F(E)$ describes the energy distribution of the electron flux passing through longitudinal position z_F. Electron flux through z_F that coincides with the simultaneous occupation of the single-electron state $|L_0\rangle$ is consequently described by applying the operator $\hat{\mathbb{P}}^\dagger_{L_0}\hat{F}\hat{\mathbb{P}}_{L_0}$. Its time- or energy-dependent expectation value is going to be denoted by $F_{L_0}(t)$ and $F_{L_0}(E)$, respectively, hence as

$$F_{L_0}(t) := \big|\langle\Psi|\hat{\mathbb{P}}^\dagger_{L_0}|t\rangle\langle t|\hat{F}|t\rangle\langle t|\hat{\mathbb{P}}_{L_0}|\Psi\rangle\big|, \tag{27}$$

$$F_{L_0}(E) := \big|\langle\Psi|\hat{\mathbb{P}}^\dagger_{L_0}|E\rangle\langle E|\hat{F}|E\rangle\langle E|\hat{\mathbb{P}}_{L_0}|\Psi\rangle\big|. \tag{28}$$

Because the initial wavefunction is not equally distributed over the entire energy range, the measured flux will depend on the energy distribution

$$D_{\Psi_0}(E) := \big|\langle\Psi_0|E\rangle\langle E|\Psi_0\rangle\big|. \tag{29}$$

The probability density for a successful inter-quantum-dot Coulombic electron capture into $|L_0\rangle$ within the infinitesimal range of total energy from E to $E + dE$ is hence given by the fraction of measured electron flux of that energy by available density distribution,

$$P_{L_0}(E) := \frac{F_{L_0}(E)}{D_{\Psi_0}(E)} \quad \text{if } D_{\Psi_0}(E) > 0. \tag{30}$$

Any evolution has to conserve the total energy E_T of the system. So, the energy transferred through a capture into $|L_0\rangle$ has to equal the energy difference between right-bound $|R\rangle$ and left-bound $|L_0\rangle$,

$$\tfrac{p_i^2}{2m^*} + E_R = E_T, \tag{31}$$

$$E_T = E_{L_0} + \tfrac{p_f^2}{2m^*}. \tag{32}$$

This is diagrammatically presented in Fig. 2(a). Despite the electronic correlations throughout the process, this means that energy

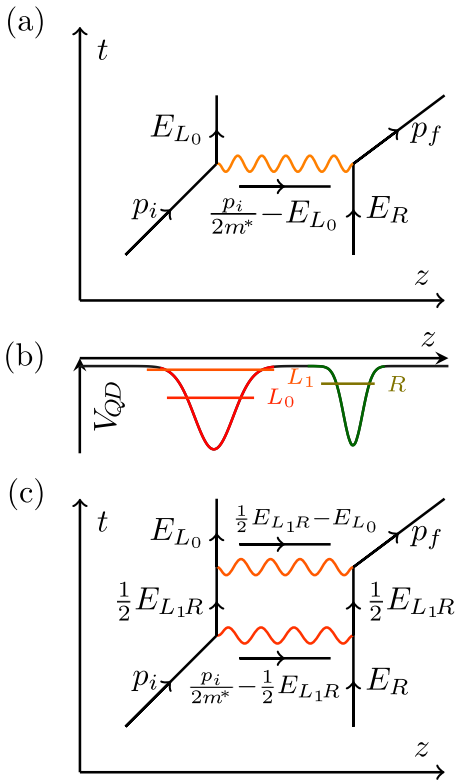

FIG. 2. (b) The binding potential V_{QD} modeling the quantum dot pair as a function of z is shown, and the energy levels of the states L_0, R, L_1 are indicated. (a) shows the diagram of direct ICEC in alignment with the binding potentials of (b). Arrows indicate the electron evolution in space and time with momentum $p_{i/f}$ or only in time when being in one state of energy $E_{L_0/R}$. The wiggled lines represent the transferred energy. (c) The representation of direct ICEC is supplemented with the representation of the resonant ICEC.

transfer is solely dependent on single-electron quantities. Under the assumption that a metastably bound two-electron excited state can be occupied which might bear at least conceptual similarities with a state of simultaneously occupied $|L_1\rangle$ and $|R\rangle$ in consequential perturbation by respective repulsion, we call this state $|L_1R\rangle$. If such a state is to be populated by the evolving state $|\Psi\rangle$ at some point in time $t \geq t_0$, energy conservation must be ensured equally. As such, only those fractions of incoming wavepacket can contribute which are appropriately energetically situated close to the energy difference [cf. see Eq. (10)] between E_{L_1R} and E_R, as depicted in diagram (c) of Fig. 2, i.e.,

$$\frac{{p_i}^2}{2m^*} + E_R = E_{L_1R}, \tag{33}$$

$$E_{L_1R} = E_{L_0} + \frac{{p_f}^2}{2m^*}. \tag{34}$$

Similarly, the kinetic energy release coinciding with a residual occupation in L_0 depends on the energy difference between E_{L_1R} and E_{L_0} as this intermediate state decays by tunneling out of the Coulomb-induced confinement barriers. Nevertheless, despite its particular dynamics via $|L_1R\rangle$, the overall excess kinetic energy remains independent of E_{L_1R} and depends solely on the single-electron quantities E_{L_0} and E_R.

If we assume ICEC to occur as an elastic scattering in the form of a direct energy transfer or impulse between the two electrons, we would expect an electron flux energetically similar to the initial energy distribution $D_\phi(\varepsilon)$. The energy distribution $D_{\Psi_0}(E_T)$ of the initial state $|\Psi_0\rangle$ is trivially separable into its electronic components, as the incoming wavepacket $|\phi\rangle$ and the right-bound electron $|R\rangle$ are at a very large distance from each other and correlative interaction is negligible,

$$D_{\Psi_0}(E_T) = D_\phi(\varepsilon) \times \delta(E_R - (E_T - \varepsilon)) \text{ for } E_T =: \varepsilon + E_R. \tag{35}$$

Due to Eqs. (7), (14), and (15), we expect the energy distribution $D_{\Psi_0}(E_T)$ to be a simple superposition of continuous contributions of free energy ε and discrete eigenenergy E_R,

$$F^{\phi}_{L_0}(\varepsilon) \propto \left|\langle E_T - E_R|\phi\rangle\right|^2 \propto \frac{p_0}{\sqrt{2m^*\varepsilon}} \frac{\exp\left[-2\frac{\sigma_z^2 p_0^2}{\hbar^2}\left(\frac{\sqrt{2m^*\varepsilon}}{p_0} - 1\right)^2\right]}{1 + \exp\left[-8\frac{\sigma_z^2 p_0^2}{\hbar^2}\right]} + \frac{p_0}{\sqrt{2m^*\varepsilon}} \frac{\exp\left[-2\frac{\sigma_z^2 p_0^2}{\hbar^2}\left(\frac{\sqrt{2m^*\varepsilon}}{p_0} + 1\right)^2\right]}{1 + \exp\left[-8\frac{\sigma_z^2 p_0^2}{\hbar^2}\right]}, \tag{36}$$

where the second term is expected to have a very small contribution near $\varepsilon = p_0^2/2m^*$.

On the other hand, assuming that the kinetic energy of the initially free wavepacket is transferred into correlation energy between the electrons, electron capture might occur initially without environmental ionization. The interaction between both bound electrons then allows a secondary energy transfer, resulting in electron tunneling out of the confinement. As this two-electron bound state thus decays, we expect the electronic flux to reflect this decay according to Eq. (10) and $F^{L_1R}_{L_0}(E_T)$ should show a Breit-Wigner shape, i.e.,

$$F^{L_1R}_{L_0}(E_T) \propto \left|\langle E_T|L_1R\rangle\right|^2 \propto \frac{\Gamma^2}{4(E_T - E_{L_1R})^2 + \Gamma^2}. \tag{37}$$

Consequently, electron capture through both processes, direct impact of $|\phi\rangle$ on $|R\rangle$ and inter-quantum-dot Coulombic decay of $|L_1R\rangle$, has to show the usual quantum mechanical superposition of amplitudes resulting in some interference term according to a complex phase difference φ between both since

$$F_{L_0}(E_T) \propto \left|K_\phi \langle E_T - E_R|\phi\rangle + K_{L_1R}\langle E_T|L_1R\rangle\right|^2. \tag{38}$$

We can therefore evaluate the probability density for the infinitesimal energy range $E_T \ldots (E_T + dE_T)$ for a successful inter-Coulombic electron capture according to Eq. (30) as

$$P_{L_0}(E_T) \propto \frac{\left|K_\phi \langle E_T - E_R|\phi\rangle + K_{L_1R}\langle E_T|L_1R\rangle\right|^2}{D_\phi(E_T - E_R)}, \quad \text{if } D_\phi(E_T - E_R) > 0. \tag{39}$$

Numerically, this definition proves to be limited to a certain confidence interval in energy for which the initial energy distribution $D_\phi(E_T - E_R)$ is confidently nonvanishing in order to avoid numerical division by 0. Note that the flux $F_{L_0}(E_T)$ can also be evaluated for regions outside the energy confidence interval.

In conclusion, the efficiency of the inter-Coulombic electron capture within an infinitesimal energy range between E_T and $E_T + dE_T$ is described by the probability density $P_{L_0}(E_T)$ expressing the ratio between successfully ionized electron density through ICEC and incident electron density within that infinitesimal energy range. The total efficiency of the device, however, is given by the direct integral of the flux density of ionized electron density through successful ICEC,

$$P^{\text{total}}_{L_0} = \frac{\int P_{L_0}(E_T) D_{\Psi_0}(E_T)\, dE_T}{\int D_{\Psi_0}(E_T)\, dE_T} = \int F_{L_0}(E_T)\, dE_T, \tag{40}$$

where the definition for F_{L_0} according to Eq. (30) and the normalization of the initial energy distribution density, $\int dE_T\, D_{\Psi_0}(E_T) = 1$, was applied. While the energy distribution density of the incident electron is just a free parameter in the initial conditions for a numerical investigation, controlling it in an experiment or a potential electronic device will be a challenge. The group velocity will primarily be controlled through the external electric field applied to the nanowire and the charge-carrier mobility of the material. In addition to being material-dependent, the mobility will also depend on the operating temperature which is difficult to control in an electronic device outside the laboratory. Moreover, controlling the distribution in energy will effectively be limited by noise arising from various sources of fluctuations due to manufacturing quality, electrical contacts, material defects, power source, or thermal fluctuations.

The overall efficiency of ICEC in an electronic device will depend on the matching or overlap between ICEC probability density $P_{L_0}(E)$ and incident energy distribution $D_{\Psi_0}(E)$. A narrow probability profile will need a narrow incident distribution. Likewise, if the energy distribution is broad due to electronic limitations, a broad probability density profile will be advantageous to use ICEC efficiently. In this study, the incident electron is used in a different way: it is kept constant to probe for $F_{L_0}(E)$ and $P_{L_0}(E)$ for a range

of energies. Therefore, we expect the total efficiency $P_{L_0}^{\text{total}}$ to remain small. Optimizing a real ICEC device for a particular chosen material would primarily mean optimizing the applied voltage, together with the width and peak value of ICEC probability density for a device at specific operating conditions.

III. COMPUTATIONAL DETAILS

We numerically apply the multiconfigurational time-dependent Hartree (MCTDH) approach with antisymmetrization to describe and propagate the quantum-mechanical two-electron wavefunction of the form[51,52]

$$\Psi(z_1,z_2,t) := \sum_{j_1,j_2=1}^{N_1,N_2} A_{j_1j_2}(t)\chi_{j_1}(z_1,t)\chi_{j_2}(z_2,t). \tag{41}$$

It contains the Hartree product of time-dependent single-particle functions (SPFs),

$$\chi_j(z,t) := \sum_{m=1}^{M} c_j^{(m)}(t) b_m(z). \tag{42}$$

Their primitive basis, $\{b_m(z)\}_{m=1}^{M}$, is given within a sine (Chebyshev) discrete variable representation (DVR) of 431 grid points each between $z = -270.0\,a_B^*$ and $+270.0\,a_B^*$ for both electronic z coordinates (see Table I). The configuration space, $N_1 \times N_2$, taken into account is of size 14×14 for the initial preparation of state and then reduced to configurations of triplet states by enforcing the identical nature of both electrons and antisymmetric coefficients through

$$A_{j_1j_2}(t) \stackrel{!}{=} -A_{j_2j_1}(t)\ \forall t. \tag{43}$$

While initially separable as both electrons are at large distance from each other, electron correlation grows with time when the electrons approach each other. Numerically, this means that the wavefunction is initially well-described by a single configuration, while with increasing time, the configuration space becomes more widely populated.

As described in the theory section, Sec. II [Eq. (25)], the initial wavefunction is prepared by an antisymmetric superposition of a free electron wavepacket of Gaussian form and the bound single-electron eigenfunction of the quantum dot localized at the right $|R\rangle$. The Gaussian wavepacket is initially centered at $Z = -125\,a_B^*$ with group momentum $p_0 = 0.335\,\hbar/a_B^*$ and root-mean-square (rms) width σ_z of $10.0\,a_B^*$, where all units are effective atomic units and scaled with respect to an effective electron mass of unity. We summarize the employed parameters concisely for better legibility and reference in Table I.

The transversal oscillator strength of the nanowire is set to $\hbar\omega_\perp = 1.0\,E_H^*$. This implies a natural length scale equal to the characteristic length scale, a_B^*, of the chosen material according to Eq. (17). The right quantum dot and interdot distance are kept constant throughout this study which ensures a constant initial wavefunction. With a rms width of $1/\sqrt{2}\,a_B^*$, such that $b_R = 1.0\,a_B^{*-2}$, the right quantum dot is set to an effective energy minimum of $D_R = 0.60\,E_H^*$ and at a distance from quantum-dot center to center of $R = 10.0\,a_B^*$ (compare Ref. 31). The left quantum dot is fixed with an effective binding energy of $D_L = 0.71\,E_H^*$ and is being varied in size between a length (i.e., double rms width) of $\mathscr{L}_L = 3.6\,a_B^*$ and $0.7\,a_B^*$.

In order to prevent unphysical reflections of the electron wavefunction at the edges of the grid and to avoid consequent self-interference, complex absorbing potentials $\hat{W}$ with

$$-i\hat{W} := -i\eta\left(\frac{|z-z_{cap}|}{a_B^*}\right)^n \times \Theta\left[-k\left(\frac{z-z_{cap}}{a_B^*}\right)\right] \tag{44}$$

of quadratic order, $n = 2$, have been placed with the Heaviside function $\Theta(z)$ at $z_{cap} = \pm 168.75\,a_B^*$.[70–73] The parameter η is computed to maximize the absorption and minimize reflection from the edges. See Table I for details.

IV. RESULTS

In this section, we intend to analyze the inter-Coulombic electron capture at various sizes $\mathscr{L}_L$ of the capturing quantum confinement by calculating the electron dynamics of this long-range energy transfer to a bound electron in another confinement within a nanowire. Before we analyze the dynamics of ICEC,

TABLE I. Collection of computational parameters of the system.

Incident electron parameters, see Eqs. (3) and (18)			
$p_0 = 0.335\,\hbar/a_B^*$	$Z = -125\,a_B^*$	$\sigma_z = 10.0\,a_B^*$	$l = 1.0\,a_B^*$
Quantum-dot-pair parameters, see Eq. (12)			
$\mathscr{L}_L \in \{0.7\,a_B^*, \ldots, 3.6\,a_B^*\}$		$D_L = 0.71\,E_H^*$	
$\mathscr{L}_R = 0.707\,a_B^*$		$D_R = 0.60\,E_H^*$	
$\mathscr{R} = 10.0\,a_B^*$			
DVR type	Grid points	z range	
Sine	431	$-270.0\,a_B^*$	$+270.0\,a_B^*$
SPF configurations		14×14, *id*	
CAP z_{cap}	η	n	k
$-168.75\,a_B^*$	$5.79 \cdot 10^{-6}\,E_H^*$	2	−1
$+168.75\,a_B^*$	$5.79 \cdot 10^{-6}\,E_H^*$	2	+1

we need to characterize the variation of static quantities with the confinement size. In Sec. IV A we thus wish to study the observed changes in single-electron eigenenergies E_{L_0} and E_{L_1} first. In accord with the nomenclature for single-electron bound states $|L_0\rangle$, $|R\rangle$, and $|L_1\rangle$, we distinguish the states $|L_0R\rangle$ and $|L_1R\rangle$ of two electrons bound within the pair of quantum confinements. We intend to discuss the electron-electron correlation energies and distances for those two-electron states. With that at hand, in Sec. IV B we plan to explain an example of the undertaken flux analysis on the full electron dynamics and eventually show six different cases of ICEC flux profiles indicating the contributions via direct ICEC and secondary ICD.

A. Quantum-size effect of stationary quantities

In the investigated range of sizes between $\mathscr{L}_L = 0.7\,a_B^*$ and $3.6\,a_B^*$, the numerical results of the dependence of single-electron eigenenergies E_{L_0}, E_R, and E_{L_1} are depicted in Fig. 3(a) as lines in violet with diamonds, in blue with triangles, and in turquoise with pentagons. As the right quantum dot has not been changed throughout, E_R is constant over the whole range of $\mathscr{L}_L$, whereas both left quantum dot energies decrease monotonically with increasing $\mathscr{L}_L$. Note that the quantum dot contains a second L_1 level only for $\mathscr{L}_L \geq 0.9a_B^*$ and that the drop in E_{L_1} is slow in the beginning until it starts to follow that of E_{L_0} from approximately $\mathscr{L}_L \geq 2.2a_B^*$ onward.

We find that the observed trend is empirically well-described by a second-order polynomial of powers of square-roots of length, $E_{L_k}(\mathscr{L}_L) = \mathscr{P}^{(k)}(\sqrt{\mathscr{L}_L}) = a_0^{(k)} + a_1^{(k)}\sqrt{\mathscr{L}_L} + a_2^{(k)}\mathscr{L}_L$, for both left-located eigenenergies E_{L_k} available in the regime. In fact, due to the limited range of bound L_1 in our sampling, the linear offset energy, $a_0^{(1)}$, can be set to zero and the two parameters, $a_1^{(1)}$ and $a_2^{(1)}$, suffice to describe the size effect efficiently for the 11 data points of negative E_{L_1} with a relative uncertainty of less than 1.3% in either parameter and a root-mean-square residual of $1.5 \times 10^{-3}E_H^*$. We find thus $a_1^{(1)} = 0.289(4)E_H^*/\sqrt{a_B^*}$ and $a_2^{(1)} = -0.199(3)E_H^*/a_B^{*2}$. Similarly, the 21 data points for L_0 are empirically described by parameters $a_0^{(0)} = 0.472(4)E_H^*$, $a_1^{(0)} = -0.864(5)E_H^*/\sqrt{a_B^*}$, and $a_2^{(0)} = 0.184(2)E_H^*/a_B^{*2}$ with respective relative uncertainties below 1.0% rms residual of $0.7 \times 10^{-3}E_H^*$.

While known analytical solutions to eigenvalue problems of quantum mechanical potentials—such as the quantum-harmonic oscillator, the infinite or finite square well, and the Pöschl-Teller or Morse potential—suggest an expansion in powers of n and $\mathscr{L}_L^{-1}$ rather than square roots of length, such a second order polynomial only yields a rms residual of $3.2 \times 10^{-3}E_H^*$ for the quantum size effect in L_0 and deviates from the numerical results in its behavior which is particularly perceptible at lower sizes around $1.0\,a_B^*$. A third order term is able to correct this behavior and to reduce the rms residual to $0.2 \times 10^{-3}E_H^*$ for L_0. It also allows a smoother transition of the L_1 eigenenergy toward zero. Nevertheless, this suggested otherwise little advantage over the simpler description in orders of $\sqrt{\mathscr{L}}$ for the investigated size range.

In Fig. 3(a), we also depict the constant total $\langle E_T\rangle$ [green line with hollow squares, cf. Eqs. (31) and (25)] as well as the energy difference $\langle E_T\rangle - E_{L_0}$ (red line with circled pluses) and the unchanged initial momentum p_0 (yellow triple line with circled crosses). From all the curves together, we can make out distinct crossing points. Just above the selected $\mathscr{L}_L$ region, the crossing of E_{L_1} and E_R as well as $\langle E_T\rangle$ is expected. Another point that was highlighted in earlier investigations on ICEC as a function of D_L is the crossing of $\langle E_T\rangle$ with $E_{L_0} - E_R$ and E_{L_1R} all together, where the highest ICEC probability due to favorable energy conditions for resonance ICEC was found.[31] Here, we only see crossing points near $\mathscr{L}_L = 1.125\,a_B^*$ where the left confinement has only one bound state. E_{L_0} crosses with E_R and $\langle E_T\rangle - E_{L_0}$ with p_0. The specialty of the system at this length can be revealed when considering the two-electron quantities as well.

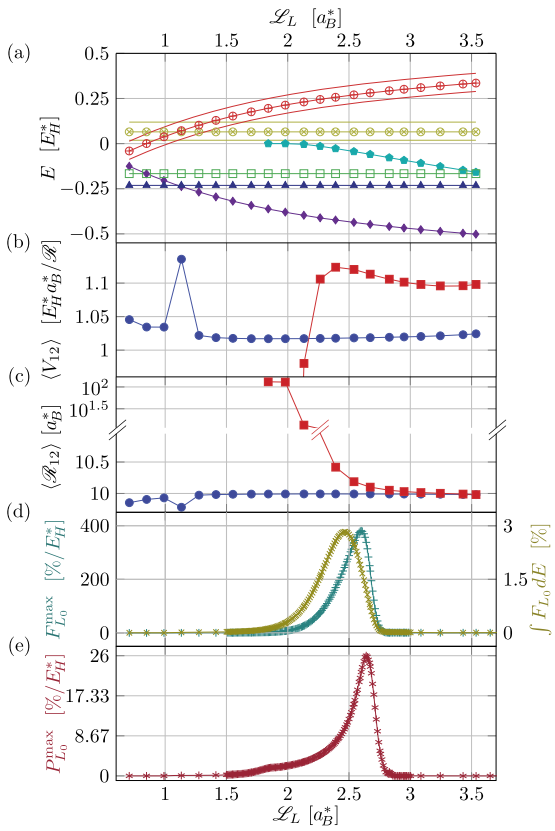

FIG. 3. The key quantities of the system of two quantum dots in a nanowire are displayed as a function of $\mathscr{L}_L$ in a_B^*. (a) Energy and momentum contributions are shown. For the single-electron energies, lines with violet diamonds represent E_{L_0}, with blue triangles E_R, and with turquoise pentagons (setting on for $\mathscr{L}_L \geq 1.84\,a_B^*$) E_{L_1}. The constant transferred energy $\langle E_T\rangle$ is shown as a green line with hollow squares. The range of available final energies $\langle E_T\rangle - E_{L_0}$ is indicated by a red line with circled pluses, and adjacent red lines mark three standard deviations $\sigma_\varepsilon^\pm = \hbar/(2m^*\sigma_z)(p_0 \pm \hbar/(4\sigma_z))$. The unchanged initial kinetic energy $p_0^2/(2m^*) \pm 3\sigma_\varepsilon^\pm$ with three standard deviations is displayed by a yellow triple line with circled crosses. (b) Coulomb interaction $\langle V_{12}\rangle_{L_kR}$ for $|L_0R\rangle$ (blue dots) and $|L_1R\rangle$ (red squares) obtained from $E_{L_kR} - E_{L_k} - E_R$ and scaled by $1/\mathscr{R}$. (c) Effective distances $\langle \mathscr{R}_{12}\rangle = \langle |z_2 - z_1|\rangle_{L_kR}$ for states as in (b). Note the scale breaking. (d) Maximal flux density $F_{L_0}^{\max}$ (turquoise cross symbol with the peak at $\mathscr{L}_L \approx 2.6\,a_B^*$) and integrated flux $\int F_{L_0} dE$ (olive plus symbol with the peak at $\mathscr{L}_L \approx 2.45\,a_B^*$) with distinct scales of the ordinate. (e) Maximal ICEC probability density $P_{L_0}^{\max}$ (purple asterisk) depending on the size $\mathscr{L}_L$ of the capturing quantum confinement.

In Fig. 3(b), we plot the expectation values of the interaction strength, the effective Coulomb energy $\langle V_{12}\rangle_{L_kR}$ as a function of $\mathscr{L}_L$. It was calculated according to $E_{L_kR} - E_{L_k} - E_R$ for the two-electron ground state $|L_0R\rangle$ (blue dots) and the resonance $|L_1R\rangle$ (red squares). In Fig. 3(c), lines with the same color code are used to depict the respective electron-electron distance $\langle\mathscr{R}_{12}\rangle_{L_kR}$ from $|L_0R\rangle$ and $|L_1R\rangle$ of (b). These quantities have been determined to quantify their difference from the estimate of $\langle V_{12}\rangle_{L_kR} \approx 1/\mathscr{R}$. For the lowest two-electron bound state of the system, $|L_0R\rangle$, the average expectation of ground state interaction strength in our sampling lies 2.75% above the approximation of $1/\mathscr{R} = 0.10\,E_H^*$. Peaking with an expectation value of $\langle V_{12}\rangle_{L_0R} = 0.1136\,E_H^*$ at a quantum-dot length $\mathscr{L}_L$ of $1.13\,a_B^*$ around where the single-electronic eigenenergies E_{L_0} and E_R cross, the limited resolution suggests a lambda transitional shape. For a narrow left quantum dot below $1.0\,a_B^*$, the expectation value appears to significantly increase as the bound electron delocalizes due to the close threshold energy. For lengths above $1.5\,a_B^*$, electronic interaction increases slowly as the separation between the quantum dots reduces together while the left quantum dot grows equally to the left. Within the investigated range, the minimal interaction strength in the two-eelctron ground state is found with $0.1017\,E_H^*$ at a longitudinal quantum-dot size of $1.84\,a_B^*$.

In comparison, the resonance state level $|L_1R\rangle$ shows a mean expectation value of interaction strength $\langle V_{12}\rangle_{L_1R}$ which is 10.58% above the approximated $1/\mathscr{R} = 0.10\,E_H^*$. It deviates from the approximate by the order of the system's kinetic energy. This estimate proves therefore only a crude approximation. From its minimal electronic interaction of $\langle V_{12}\rangle_{L_1R} = 0.1096\,E_H^*$ at a left quantum dot size of $\mathscr{L}_L = 3.24\,a_B^*$, electronic repulsion increases with E_{L_1} as the quantum dot narrows. It climaxes with $\langle V_{12}\rangle_{L_1R} = 0.1124\,E_H^*$ at a size $\mathscr{L}_L$ of $2.39\,a_B^*$ where the gain in eigenenergy is balanced by the increasingly available localization range as the quantum dot potential spreads with length $\mathscr{L}_L$. Electronic interaction drops therefore steeply around the zero transition of $|L_1\rangle$ as the wavefunction extends toward $-\infty$ when the eigenvalue is being pushed out of the binding potential. Similar to the electronic repulsion in the ground state $|L_0R\rangle$, we observe a slow repulsive rise of $\langle V_{12}\rangle_{L_1R}$ for larger sizes $\mathscr{L}_L$ as the quantum-dot barrier reduces until the quantum-dot pair amalgamates.

While the electrons are bound by the respective quantum-dot potentials, we expect electronic repulsion to polarize the individual quantum dot such that the average electron densities are slightly shifted and one could naïvely assume the repulsive force to hold the electrons outwards from their original noninteracting equilibrium position, $\langle|z_2 - z_1|\rangle \gtrsim \mathscr{R}$. Surprisingly, we find the expectation value of the interelectronic distance [see Fig. 3(c)] in the ground state $|L_0R\rangle$ continuously slightly smaller than the distance between the respective quantum-dot centers with a mean electron-electron distance $\langle\mathscr{R}_{12}\rangle_{L_0R}$ of $9.995(12)\,a_B^*$ with the uncertainty within the last digits given in parentheses. We particularly observe a general reduction of electronic distance at $\mathscr{L}_L < 2\,a_B^*$ and an intermediate drop at $\mathscr{L}_L = 1.13(15)\,a_B^*$ as the left and right-localized eigenenergies cross and direct tunneling opens up the available space. This behavior of $\langle\mathscr{R}_{12}\rangle_{L_0R}$ partially counteracts the trend in $\langle V_{12}\rangle_{L_0R}$ of Fig. 3(b).

For the two-electron excited state $|L_1R\rangle$, we find a strong quantum-size dependence of the expectation value of the interelectronic distance. We measure an expectation value $\langle\mathscr{R}_{12}\rangle_{L1R}$ of $9.982(4)\,a_B^*$ at left quantum-dot size $\mathscr{L}_L = 3.50\,a_B^*$ and $\langle\mathscr{R}_{12}\rangle_{L_1R} = 10.25(7)\,a_B^*$ at $\mathscr{L}_L = 2.50\,a_B^*$. Narrowing the left quantum dot further raises the interelectronic distance with the eigenenergy E_{L_1}. This opens up a wider range between the potential reflection points as the potential approaches the continuum such that $\langle\mathscr{R}_{12}\rangle_{L_1R} = (19 \pm 6)\,a_B^*$ at $\mathscr{L}_L = 2.125\,a_B^*$ before the localization of $|L_1\rangle$ breaks down. The overall trend is inverse to the behavior of $\langle V_{12}\rangle_{L_1R}$. Only in the range $2.39\,a_B^* < \mathscr{L}_L < 3.20\,a_B^*$, interestingly, the system simultaneously allows an increased expectation value of the Coulomb interaction $\langle V_{12}\rangle_{L_1R} > \frac{1}{\mathscr{R}}$ despite an expanded expectation value in electron-electron distance $\langle\mathscr{R}_{12}\rangle_{L_1R} > \mathscr{R}$ for most of the investigated quantum-dot-size range before the vanishing of $|L_1\rangle$ into the continuum.

Figure 3(d) depicts the integral of $F_{L_0}(E)$ with respect to the energy E, and it represents the overall efficiency of the electronic device for the chosen initial conditions and geometry. In panel (e), the maximum probability density of ICEC (obtained for a specific system energy) is plotted against the quantum confinement $\mathscr{L}_L$. These maximum values can be located in Fig. 5 as the values of the peaks of P_{L_0} (blue dashed lines, ordinate scale on right) for the quantum confinements indicated. A detailed discussion of these curves will follow in Subsection IV B within the context of the ICEC dynamics.

B. ICEC dynamics

Having investigated single-electron eigenenergies of the system and electron-electron correlated two-electron intermediate states as precursors to analyze the full ICEC dynamics, we would like to discuss with $\mathscr{L}_L = 2.83\,a_B^*$ an exemplary case of the flux analysis at this point. Investigating the time-dependent spatial probability density $|\Psi(t)|^2$ based on Eqs. (25) and (41) as depicted in the lower panel of Fig. 4, we find that for the first times up to $210\,\hbar/E_H^*$ the incoming electron approaches the right-bound one coming from the negative z direction. During this time, we observe a broadening of the incoming wavepacket in time due to its dispersion. From impact, we observe a spray of electron probability density leaving in the positive z direction with increased velocity in comparison with the incoming one notable at the steeper slope $\Delta z/\Delta t$. At the same time, we observe interference ridges in the negative z direction, as fractions of the incoming wavefront are being reflected back to the left and interfere with fractions still traveling toward the double confinement. Note that immediately from the impact, we also observe a double line at the position of the left quantum dot indicating a binding to the left-excited state $|L_1\rangle$. The first wave of right-bound electron release terminates around $550\,\hbar/E_H^*$. We further observe a revival of a second wave of right-bound electron release around $650\,\hbar/E_H^*$ to $1050\,\hbar/E_H^*$. At the same time, we note a loss of resolution in the left-bound double peak which indicates consecutively with the simultaneous right-bound ionization an active ICD process. Both of those electron probability waves were measurable as flux of time $F_{L_0}(t)$ [Eq. (27) and upper panel of Fig. 4] in coincidence with an occupied left-bound ground state $|L_0\rangle$ with maximum at time $550\,\hbar/E_H^*$ and therefore confirm to be the result of an inter-quantum-dot Coulombic electron capture.

In order to consequently investigate the confinement-size dependent ICEC through the measured flux, we Fourier transform

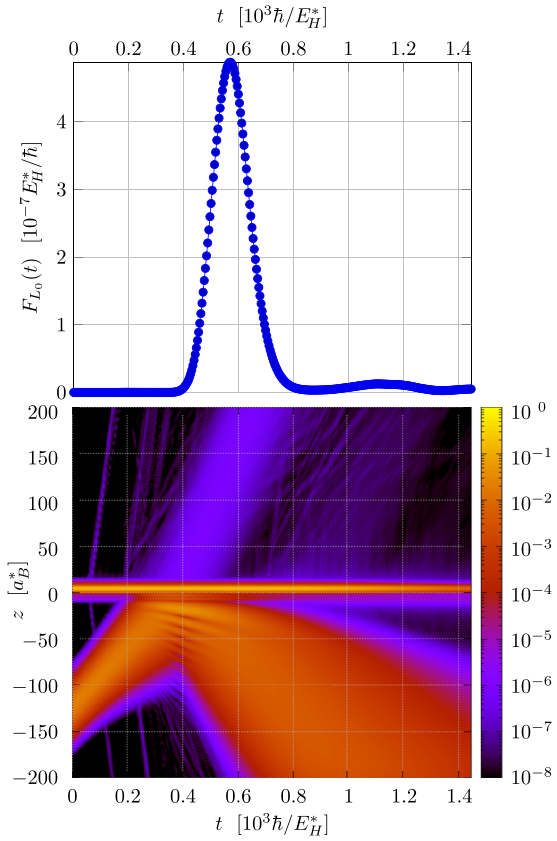

FIG. 4. Lower panel: evolution of the spatial probability density $|\Psi(t)|^2$ with time [see Eqs. (25) and (41)]. Upper panel: time-dependent electron flux $F_{L_0}(t)$ through the wire at longitudinal position z_F in coincidence with the capture of electron density in the left quantum dot's ground state $|L_0\rangle$ for the case of $\mathscr{L}_L = 2.83\,a_B^*$.

the measured electron release in time to arrive at an energy dependent flux profile $F_{L_0}(E)$ [Eq. (38)]. The incident electron possesses an initial energy distribution (depicted as a black dotted line in Fig. 5) which is independent of the size of quantum confinement $\mathscr{L}_L$. However, the confinement size affects the available eigenenergies E_{L_0} and E_{L_1} into which the incoming electron can be captured. ICEC allows the electron capture by transferring the excess energy to a bound electron on the neighboring quantum confinement. This second electron is being released, and the electron flux density $F_{L_0}(E)$ related to a capture into the ground state L_0 can be measured in dependence of the system energy E. Consequently, measuring the electron flux density F_{L_0} of ionization at occupied L_0 is a direct measure for the inter-Coulombic electron capture and can thus be called ICEC flux density in brief. The ICEC flux density is shown by a solid red line belonging to the left ordinate in Fig. 5 for several quantum confinement sizes $\mathscr{L}_L$. If ICEC works through direct impulse transfer between the electrons, one observes an energy distribution of the released flux density which is of the same character as the initial distribution. If ICEC goes through a two-center decay process known as ICD, the measured electron flux density shows a Lorentz shape. We find that both subprocesses contribute and can fit their superposition to the measured electron flux density. The fit is shown by a dark gray dashed-dotted line overlaying the measured electron flux.

The capturing quantum confinement region in this study can bind an electron to its ground state $|L_0\rangle$ or its excited state $|L_1\rangle$. The interacting neighbor is initially charged in state $|R\rangle$ of energy E_R between E_{L_0} and E_{L_1}. It has been discussed in Sec. II that this energy transfer enabling capture into $|L_0\rangle$ leads to the ionization of the partner electron initially bound in $|R\rangle$. It was further shown theoretically in Sec. II that electron capture into $|L_0\rangle$ can occur by direct impulse from the incident electron onto the ionized partner or by capture into an intermediate state where both electrons are bound in their respective confinement before decaying by ionization through a secondary ICD to a single bound electron in the state $|L_0\rangle$. The ionization flux densities related to these subprocesses depend differently on the energy of the system. We expect the overall ICEC flux density $F_{L_0}(E)$ as a function of the total energy E of the system to show a superposition of both characteristic contributions.

The initial conditions are determined by the energy density distribution of the incident electron and the bound electron in $|R\rangle$. They are kept constant, resulting in a constant overall initial energy distribution $D_{\Psi_0}(E)$. The probability density of successful ICEC within the infinitesimal energy range $E\ldots dE$ of the system is denoted by $P_{L_0}(E)$ and generally given by the ratio of ICEC flux density $F_{L_0}(E)$ by available initial energy density $D_{\Psi_0}(E)$ [see Eq. (30)]. Nevertheless, this definition can only be evaluated for energies with initial energy density confidently larger than 0 where division by numerically vanishing values can be avoided. The ICEC probability density $P_{L_0}(E) := F_{L_0}(E)/D_{\Psi_0}(E)$ (shown as a blue dashed line with an associated right ordinate) can be calculated within the significant interval of D_{Ψ_0} to compensate for the dependence on the initial energy distribution. The ICEC probability density is dominated by the contribution from direct impulse for large quantum confinements shown in the top left diagram for $\mathscr{L}_L = 2.95\,a_B^*$ when ICD lies outside the significant energy range. ICD grows and dominates within the significant energy range as shown in the bottom left and the top middle diagram for $\mathscr{L}_L = 2.83\,a_B^*$ and $2.77\,a_B^*$, respectively. As the confinement size is further reduced, the contributions of ICD and direct impulse superpose constructively to increase and broaden the probability density distribution shown for $\mathscr{L}_L = 2.72\,a_B^*$ in the middle bottom and $\mathscr{L}_L = 2.54\,a_B^*$ in the top right diagram. Narrowing the quantum confinement further tips the ICD resonance energy beyond the energy of maximal energy distribution which broadens the probability density considerably but impedes its maximum as shown in the bottom right panel for $\mathscr{L}_L = 2.39\,a_B^*$. Already for the discussed geometry with $\mathscr{L}_L = 2.83\,a_B^*$ in the bottom left panel of Fig. 5, we observe as expected a superposition in the electron flux profile of a Breit-Wigner resonance shape (left peak) and an energy distribution related to a normally distributed momentum (right peak). The flux profile fits expectations according to Eq. (38) (see Fig. 5, gray solid line beneath the red one, left axis labels). As discussed, we can attribute the Breit-Wigner or Lorentzian contribution according to Eq. (10) to a decay process of an intermediate state which energetically bears the energy signature of a double-electronic occupation of $|L_1R\rangle$ with electron-electron correlation energy. We further find that the other

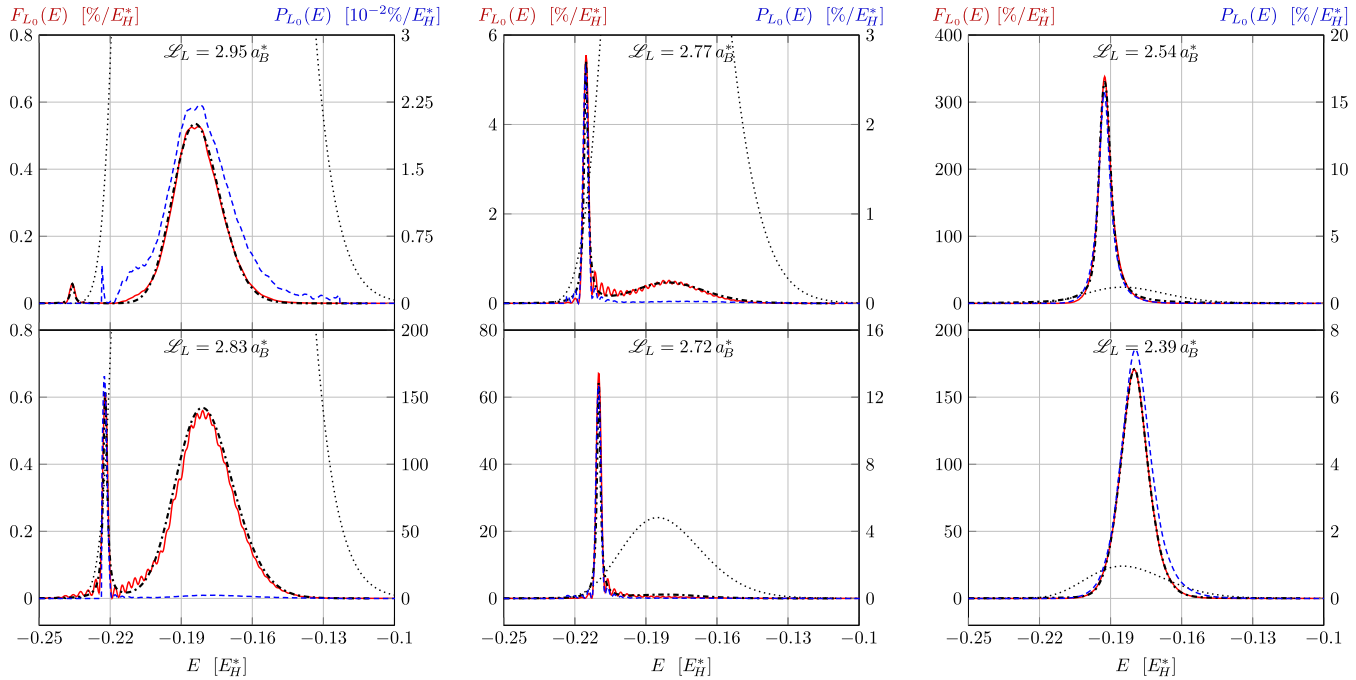

FIG. 5. Electron dynamics results for the ICEC process are shown for different quantum dot confinement lengths $\mathscr{L}_L$ with values $2.95\,a_B^*$ (top left), $2.83\,a_B^*$ (bottom left), $2.77\,a_B^*$ (top middle), $2.72\,a_B^*$ (bottom middle), $2.54\,a_B^*$ (top right), and $2.39\,a_B^*$ (bottom right). ICEC ionizes a nearby bound electron by long-range energy transfer while capturing the incident electron in energy level L_0. This flux of ionization F_{L_0} is measured (red solid line, ordinate scale on the left of each graph) and indicates two subprocesses centered at different system energies. Accordingly, ICEC can occur by direct impulse between the captured and the ionized electron contributing to F_{L_0} by a Gaussian (contribution centered at $-0.185\,E_H^*$ clearly visible as a red line for $\mathscr{L}_L$ above $2.72\,a_B^*$, left panels and the middle top panel), or it can occur by electron capture into an excited two-electron state with secondary ICD which contributes to F_{L_0} with a Breit-Wigner profile (narrow contribution centered at different energies depending on the quantum size effect and $\mathscr{L}_L$, clearly distinguishable for $\mathscr{L}_L$ above $2.72\,a_B^*$, left panels and the middle top panel; otherwise superimposed). A fit of this superposition of both processes is shown as a dark gray dashed-dotted line in agreement with the measured flux (red solid line). In all cases, an incident probing wavepacket of Gaussian shape is used with energy distribution density D_{Ψ_0} as a function of total energy E indicated by a black dotted line (absolute scale) constantly centered at $-0.185\,E_H^*$. The ratio $P_{L_0}(E) = F_{L_0}(E)/D_\Psi(E)$ is indicated as a blue dashed line and the ordinate axis on the right-hand side of all graphs. It reflects the ICEC probability density which is numerically well-defined for energy regions of significant incident electron density ($-0.23\,E_H^* \lesssim E \lesssim -0.12\,E_H^*$). Note that the scale of the ICEC probability density for the left panels is 2 orders of magnitude smaller than that for the other four graphs because the ICD resonance lies at the low-energy edge of the probing wavepacket.

contribution coincides with the shape of the initial free wavepacket according to Eq. (7).

While the panels of Fig. 5 show flux profiles for particular confinement sizes, Fig. 6 compares their intensities and maximal positions directly. As we pass through the geometries along decreasing $\mathscr{L}_L$, the resonance energy for the ICD decay varies with the quantum-size effect, while the wavepacket energy distribution is a constant throughout our study (thin dotted lines in Fig. 5). As a result, the $F(E)$ maxima of ICD resonances lie at different energies than the wavepacket maximum but are modulated in maximal intensity by the underlying shape of the wavepacket.

As the flux profile exhibits the usual quantum mechanical superposition according to Eq. (38), we note the variation in composed shape of the flux profile as the ICD resonance passes through the contribution of direct impulse. As both energies get closer, the process signatures become harder to distinguish as can be seen from the last three panels of Fig. 5. As they overlap, the flux profile appears to be of the Breit-Wigner shape at first glance in accord with former predictions[31] but remains a superposition of both processes. Nevertheless, it is still numerically obvious that a decay-describing Lorentzian function can only partially account for the entire shape. We note that the impulse related contribution exhibits a dispersed root-mean-square width with respect to the initial minimum-uncertainty wavepacket which we attribute to the time passed between the release of the initial wavepacket and the impact on the initially bound electron. Last but not least, we observe that for the extended range of confinement sizes above $\mathscr{L}_L = 2.83\,a_B^*$ (Fig. 3, top left), major contributions to the flux from the ICD subprocess lie partially outside the confidence interval provided by the initial energy distribution. The definition of the electron capture probability equation (39) shown as a blue dashed line in Fig. 5 with the ordinate on the right hand side is therefore of limited use in cases where the flux maximum position differs largely from the energy distribution maximum. As the capture probability partially encrypts the signature of the probing wavepacket, so does to a lesser extent the maximum of released electron flux density. In the overview of

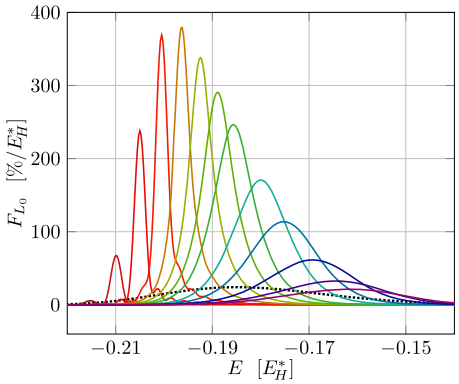

FIG. 6. The capture of an incident electron into $|L_0\rangle$ releases a nearby electron initially bound to the state $|R\rangle$ and is characterized by magnitude, shape, and average energy of the ICEC ionization flux density F_{L_0} (solid lines) as a function of the total energy E and the size $\mathscr{L}_L$ shown as consecutive set of curves. The dark red curve with peak maximum $F_{L_0}^{\max} = 5.5\,\%/E_H^*$ barely visible at $E = -0.215\,E_H^*$ (to the left) belongs to $\mathscr{L}_L = 2.77\,a_B^*$, and the second from the left with peak maximum $F_{L_0}^{\max} = 67.1\,\%/E_H^*$ at $E = -0.210\,E_H^*$ belongs to $\mathscr{L}_L = 2.72\,a_B^*$. With decreasing confinement sizes $\mathscr{L}_L$, the width of the ICEC flux profile $F_{L_0}(E)$ broadens and the peak moves gradually to higher total energies E. The dark blue-violet curve second from the right with a peak maximum of $F_{L_0}^{\max} = 33.4\,\%/E_H^*$ at $E = -0.165\,E_H^*$ belongs to a confinement size of $\mathscr{L}_L = 2.15\,a_B^*$ and the very right violet line with peak $F_{L_0}^{\max} = 21.4\,\%/E_H^*$ at $E = -0.162\,E_H^*$ belongs to $\mathscr{L}_L = 2.10\,a_B^*$. The maximal peak in ICEC flux is achieved with $F_{L_0}^{\max} = 379.4\,\%/E_H^*$ at $E = -0.196\,E_H^*$ for a confinement size of $\mathscr{L}_L = 2.58\,a_B^*$ and shown in orange. It is offset by $-0.011\,E_H^*$ to the maximum of the initial energy distribution D_{Ψ_0} which is indicated in absolute scale by the dashed black line with maximum at $E = -0.185\,a_B^*$.

Fig. 6, we hence used $F(E)$. In addition, in Fig. 3(d), we plot the electron flux density and its integral as a function of confinement size $\mathscr{L}_L$. One can observe how ICEC becomes negligible outside a certain region of $\mathscr{L}_L$ and corresponding energies E. For $\mathscr{L}_L < 2.11\,a_B^*$, no $|L_1\rangle$ level exists and this corresponds to flux maxima at larger energies $E > -0.16\,E_H^*$, whereas in the inverse case for $\mathscr{L}_L > 2.77\,a_B^*$ at energies $E < -0.21\,E_H^*$ the two ICEC pathways fail to overlay in energy. In between, maximal fluxes are reached for energetically overlapping channels which not only agrees with former results[31] but also reveals further the detailed reason. Note that of all quantities $\langle V_{12}\rangle$ and $\int F_{L_0}(E)dE$ in Figs. 3(b) and 3(d) align most closely indicating that the flux probability follows tightly the Coulomb interaction.

V. CONCLUSION

In this study, we investigated the quantum-size effect of inter-Coulombic electron capture (ICEC) within an established linear model of a nanowire. A free-moving electron is hereby being confined into an embedded quantum dot through long-range energy transfer onto a bound electron in a nearby confinement. We used electron-dynamics computations to analyze the ionization flux density coinciding with a ground state population in the capturing quantum confinement region. We were able to identify and distinguish contributions of direct impulse and conversion of kinetic energy to correlation energy with secondary intercoulombic decay (ICD). The significant range of capturing quantum confinement sizes for successful ICEC lies between 1.8 and 2.8 a_B^*. For the established system and its initial conditions, the maximal ICEC related ionization flux density of 379.4 %/E_H^* was found at a confinement size of 2.58 a_B^*. The maximal overall ICEC related ionization flux of 2.85% was found at a confinement size of 2.46 a_B^*. It was found that ICEC is very size-sensitive above the optimal confinement size where it becomes highly energy selective. At the same time, it showed less sensitivity for confinement sizes smaller than the optimum where it was generally active for a broader range of incident electron energy and was therefore less energy selective. The quantum confinement size for the optimal ICEC probability density has thus been found to be highly asymmetrical where the ICD resonance lies at slightly lower energy than the group momentum of the incident electron. Hence, the highest peak in ICEC probability density is 25.4 %/E_H^* at 2.63 a_B^*.

The optimal ICEC probability density lies within an energy range where the incident kinetic energy and the energy of the excited bound level negate each other. The optimal probability density is found where $|E_{L_1}| = \varepsilon_i - 1.5\sigma_\varepsilon^-$ in this study. It is yet unclear whether this indicates a more general criterion for ICEC or a limitation in resolution by the probing incident electronic wavepacket. Similarly, the absolute "efficiency" of ICEC remains a multifaceted difficult question considering a potential electronic device. While the dependence on the initial energy distribution is taken out of the ICEC probability density, the overall process efficiency remains dependent on the initial conditions. The group velocity of the incident electron will probably be controllable via voltage and current characteristics of the particular device, but thermal effects as well as noise from electrical contacts and the power source will limit the possible control over the energy distribution of the incident electron. In that case, the overall ICEC efficiency may depend more strongly on the width of the probability density function than on its particular maximum.

While the ICEC related electron flux density has served well in this study to distinguish between the reaction pathways and their respective contributions at different quantum-dot sizes, its direct relation to the ICEC probability density is less obvious. Its integral which represents the total efficiency remains of less interest if the incident wavepacket is chosen to be broadranged to probe a larger region of energies. We thus intend to investigate energy relations optimizing or restricting the ICEC probability density in a following study.[57] The first hint in that direction was already obtained here: We numerically evaluated the size dependence of single-electron eigenstates for the investigated confinement sizes, expectation values of electron-electron distance, and Coulomb interaction energy of correlation-perturbed doubly bound two-electron states and found that the Coulomb interaction and the integrated flux density follow each other.

ACKNOWLEDGMENTS

The authors would like to express their gratitude for funding by the Volkswagen foundation through Freigeist Grant No. 89525, and E.R.B. was additionally funded by the HZB Summer Student program. F.M.P. acknowledges SECYT-UNC and CONICET (No. PIP-11220150100327CO) for partial financial support. The authors thank Victoria Noel.

REFERENCES

[1]G. Moore, "Moore's law at 40," in *Understanding Moore's Law: Four Decades of Innovation*, edited by D. Brock (Chemical Heritage Foundation, 2006), Chap. 7, pp. 67–84.

[2]Computer companies raced to be the first to release a revolutionizing *486* personal computer toward the end of 1989. Based on the Intel 80 486 microprocessor, these computers had already passed the 800-nm node and were to make personal computers *affordable* (with prices between $10 000 and $20 000 at their launch).

[3]P. H. Lewis, "The executive computer; the race to market a 486 machine," https://www.nytimes.com/1989/10/22/business/the-executive-computer-the-race-to-market-a-486-machine.html, New York Times of October 22, 1989.

[4]W. Lambrechts, S. Sinha, J. A. Abdallah, and J. Prinsloo, *Extending Moore's Law through Advanced Semiconductor Design and Processing Techniques* (CRC Press/Taylor & Francis Group, Boca Raton, FL, 2019).

[5]K. Mistry, C. Allen, C. Auth, B. Beattie, D. Bergstrom, M. Bost, M. Brazier, M. Buehler, A. Cappellani, R. Chau, C. Choi, G. Ding, K. Fischer, T. Ghani, R. Grover, W. Han, D. Hanken, M. Hattendorf, J. He, J. Hicks, R. Huessner, D. Ingerly, P. Jain, R. James, L. Jong, S. Joshi, C. Kenyon, K. Kuhn, K. Lee, H. Liu, J. Maiz, B. McIntyre, P. Moon, J. Neirynck, S. Pae, C. Parker, D. Parsons, C. Prasad, L. Pipes, M. Prince, P. Ranade, T. Reynolds, J. Sandford, L. Shifren, J. Sebastian, J. Seiple, D. Simon, S. Sivakumar, P. Smith, C. Thomas, T. Troeger, P. Vandervoorn, S. Williams, and K. Zawadzki, in *IEEE International Electron Devices Meeting (IEDM)* (IEEE, 2007), p. 247.

[6]S. Natarajan, M. Agostinelli, S. Akbar, M. Bost, A. Bowonder, V. Chikarmane, S. Chouksey, A. Dasgupta, K. Fischer, Q. Fu, T. Ghani, M. Giles, S. Govindaraju, R. Grover, W. Han, D. G. Hanken, E. Haralson, M. Haran, M. Heckscher, R. Heussner, P. Jain, R. James, R. Jhaveri, I. Jin, H. Kam, E. Karl, C. L. Kenyon, M. Y. Liu, Y. Luo, R. Mehandru, S. Morarka, L. Neiberg, P. Packan, A. Paliwal, C. Parker, P. Patel, R. Patel, C. Pelto, L. C. Pipes, P. Plekhanov, M. Prince, S. Rajamani, J. Sandford, B. Sell, S. Sivakumar, P. Smith, B. Song, K. Tone, T. Tröger, J. Wiedemer, M. Yang, and K. Zhang, in *IEEE International Electron Devices Meeting (IEDM)* (IEEE, 2014), 3.7.1.

[7]Apple introduces iphone xr, https://www.apple.com/newsroom/2018/09/apple-introduces-iphone-xr/, Apple, Inc. Press Release of September 12 (2018).

[8]Huawei launches kirin 980, the world's first commercial 7 nm soc, https://consumer.huawei.com/en/press/news/2018/huawei-launches-kirin-980-the-first-commercial-7nm-soc/, Press Release of August 31 (2018).

[9]E. Vogel, Nat. Nanotechnol. **2**, 25 (2007).

[10]S. Datta, Nat. Electron. **1**, 500 (2018).

[11]R. Rossetti, J. L. Ellison, J. M. Gibson, and L. E. Brus, J. Chem. Phys. **80**, 4464 (1984).

[12]A. P. Alivisatos, J. Phys. Chem. **100**, 13226 (1996).

[13]A. P. Alivisatos, Science **271**, 933 (1996).

[14]F. Kuemmeth, K. I. Bolotin, S.-F. Shi, and D. C. Ralph, Nano Lett. **8**, 4506 (2008).

[15]L. Brus, J. Phys. Chem. **90**, 2555 (1986).

[16]N. N. Ledentsov, Semicond. Sci. Technol. **26**, 014001 (2011).

[17]F. Meinardi, H. McDaniel, F. Carulli, A. Colombo, K. A. Velizhanin, N. S. Makarov, R. Simonutti, V. I. Klimov, and S. Brovelli, Nat. Nanotechnol. **10**, 878 (2015).

[18]M. Mansuripur, *Nonlinear Optics* (OMA2, 2011).

[19]H.-W. Chen, J.-H. Lee, B.-Y. Lin, S. Chen, and S.-T. Wu, Light: Sci. Appl. **7**, 17168 (2018).

[20]Z. Qian, S. Kang, V. Rajaram, C. Cassella, N. E. McGruer, and M. Rinaldi, Nat. Nanotechnol. **12**, 969 (2017).

[21]W. Luo, J. Lai, D. Lu, C. Du, Y. Liu, S. Gong, D. Shi, and C. Guo, J. Phys. B: At., Mol. Opt. Phys. **45**, 035402 (2012).

[22]N. Singh, A. Agarwal, L. K. Bera, T. Y. Liow, R. Yang, S. C. Rustagi, C. H. Tung, R. Kumar, G. Q. Lo, N. Balasubramanian, and D. Kwong, IEEE Electron Device Lett. **27**, 383 (2006).

[23]R. Huang, R. Wang, J. Zhuge, C. Liu, T. Yu, L. Zhang, X. Huang, Y. Ai, J. Zou, Y. Liu, J. Fan, H. Liao, and Y. Wang, in *IEEE Custom Integrated Circuits Conference (CICC)* (IEEE, 2011), p. 1.

[24]D. B. Suyatin, V. Jain, V. A. Nebol'sin, J. Trägårdh, M. E. Messing, J. B. Wagner, O. Persson, R. Timm, A. Mikkelsen, I. Maximov, L. Samuelson, and H. Pettersson, Nat. Commun. **5**, 3221 (2014).

[25]R. Leturcq, C. Stampfer, K. Inderbitzin, L. Durrer, C. Hierold, E. Mariani, M. G. Schultz, F. von Oppen, and K. Ensslin, Nat. Phys. **5**, 327 (2009).

[26]J. Salfi, S. Roddaro, D. Ercolani, L. Sorba, I. Savelyev, M. Blumin, H. E. Ruda, and F. Beltram, Semicond. Sci. Technol. **25**, 024007 (2010).

[27]S. Roddaro, A. Pescaglini, D. Ercolani, L. Sorba, and F. Beltram, Nano Lett. **11**, 1695 (2011).

[28]W. G. van der Wiel, S. De Franceschi, J. M. Elzerman, T. Fujisawa, S. Tarucha, and L. P. Kouwenhoven, Rev. Mod. Phys. **75**, 1 (2002).

[29]F. M. Pont, A. Bande, and L. S. Cederbaum, Phys. Rev. B **88**, 241304(R) (2013).

[30]A. Bande, F. M. Pont, K. Gokhberg, and L. S. Cederbaum, EPJ Web Conf. **84**, 07002 (2015).

[31]F. M. Pont, A. Bande, and L. S. Cederbaum, J. Phys.: Condens. Matter **28**, 075301 (2016).

[32]K. Gokhberg and L. S. Cederbaum, J. Phys. B: At., Mol. Opt. Phys. **42**, 231001 (2009).

[33]K. Gokhberg and L. S. Cederbaum, Phys. Rev. A **82**, 052507 (2010).

[34]N. Sisourat, T. Miteva, J. D. Gorfinkiel, K. Gokhberg, and L. S. Cederbaum, Phys. Rev. A **98**, 020701(R) (2018).

[35]L. S. Cederbaum, J. Zobeley, and F. Tarantelli, Phys. Rev. Lett. **79**, 4778 (1997).

[36]U. Hergenhahn, J. Electron Spectrosc. Relat. Phenom. **184**, 78 (2011).

[37]T. Jahnke, J. Phys. B: At., Mol. Opt. Phys. **48**, 082001 (2015).

[38]A. Bande, K. Gokhberg, and L. S. Cederbaum, J. Chem. Phys. **135**, 144112 (2011).

[39]I. Cherkes and N. Moiseyev, Phys. Rev. B **83**, 113303 (2011).

[40]A. Bande, F. M. Pont, P. Dolbundalchok, K. Gokhberg, and L. S. Cederbaum, EPJ Web Conf. **41**, 04031 (2013).

[41]A. C. LaForge, M. Shcherbinin, F. Stienkemeier, R. Richter, R. Moshammer, T. Pfeifer, and M. Mudrich, Nat. Phys. **15**, 247 (2019).

[42]R. A. Wilhelm, E. Gruber, J. Schwestka, R. Kozubek, T. I. Madeira, J. P. Marques, J. Kobus, A. V. Krasheninnikov, M. Schleberger, and F. Aumayr, Phys. Rev. Lett. **119**, 103401 (2017).

[43]X. Ren, E. Wang, A. D. Skitnevskaya, A. B. Trofimov, K. Gokhberg, and A. Dorn, Nat. Phys. **14**, 1062 (2018).

[44]S. Xu, D. Guo, X. Ma, X. Zhu, W. Feng, S. Yan, D. Zhao, Y. Gao, S. Zhang, X. Ren, Y. Zhao, Z. Xu, A. Dorn, L. S. Cederbaum, and N. V. Kryzhevoi, Angew. Chem., Int. Ed. **57**, 17023 (2018).

[45]V. Averbukh and L. S. Cederbaum, Phys. Rev. Lett. **96**, 053401 (2006).

[46]T. Goldzak, L. Gantz, I. Gilary, G. Bahir, and N. Moiseyev, Phys. Rev. B **91**, 165312 (2015).

[47]T. Goldzak, L. Gantz, I. Gilary, G. Bahir, and N. Moiseyev, Phys. Rev. B **93**, 045310 (2016).

[48]J. Titze, M. S. Schöffler, H.-K. Kim, F. Trinter, M. Waitz, J. Voigtsberger, N. Neumann, B. Ulrich, K. Kreidi, R. Wallauer, M. Odenweller, T. Havermeier, S. Schössler, M. Meckel, L. Foucar, T. Jahnke, A. Czasch, L. P. H. Schmidt, O. Jagutzki, R. E. Grisenti, H. Schmidt-Böcking, H. J. Lüdde, and R. Dörner, Phys. Rev. Lett. **106**, 033201 (2011).

[49]H.-K. Kim, H. Gassert, M. S. Schöffler, J. N. Titze, M. Waitz, J. Voigtsberger, F. Trinter, J. Becht, A. Kalinin, N. Neumann, C. Zhou, L. P. H. Schmidt, O. Jagutzki, A. Czasch, H. Merabet, H. Schmidt-Böcking, T. Jahnke, A. Cassimi, and R. Dörner, Phys. Rev. A **88**, 042707 (2013).

[50]S. Yan, P. Zhang, X. Ma, S. Xu, B. Li, X. L. Zhu, W. T. Feng, S. F. Zhang, D. M. Zhao, R. T. Zhang, D. L. Guo, and H. P. Liu, Phys. Rev. A **88**, 042712 (2013).

[51]H.-D. Meyer, U. Manthe, and L. S. Cederbaum, Chem. Phys. Lett. **165**, 73 (1990).

[52]U. Manthe, H.-D. Meyer, and L. S. Cederbaum, J. Chem. Phys. **97**, 3199 (1992).

[53]M. H. Beck, A. Jäckle, G. A. Worth, and H.-D. Meyer, Phys. Rep. **324**, 1 (2000).

[54]*Multidimensional Quantum Dynamics*, edited by H.-D. Meyer, F. Gatti, and G. A. Worth (Wiley-VCH, Weinheim, 2009).

[55]P. Dolbundalchok, D. Peláez, E. F. Aziz, and A. Bande, J. Comput. Chem. **37**, 2249 (2016).

[56]F. Weber, E. F. Aziz, and A. Bande, J. Comput. Chem. **38**, 2141 (2017).
[57]F. M. Pont, A. Molle, E. R. Berikaa, S. Bubeck, and A. Bande, "Generous Geometry-Dependence of the Inter-Coulombic Electron Capture" (unpublished).
[58]O. Rosas-Ortiz, N. Fernández-García, and S. Cruz y Cruz, AIP Conf. Proc. **1077**, 31 (2008).
[59]N. Bohr, London, Edinburgh, Dublin Philos. Mag. J. Sci. **26**, 476 (1913).
[60]D. R. Hartree, Math. Proc. Cambridge Philos. Soc. **24**, 89–110 (1928).
[61]R. T. Tung, Appl. Phys. Rev. **1**, 011304 (2014).
[62]W. Shockley, Bell Syst. Tech. J. **28**, 435 (1949).
[63]H. Kroemer, Proc. IEEE **70**, 13 (1982).
[64]S. Lee, O. L. Lazarenkova, P. von Allmen, F. Oyafuso, and G. Klimeck, Phys. Rev. B **70**, 125307 (2004).
[65]I. A. Digdaya, G. W. P. Adhyaksa, B. J. Trześniewski, E. C. Garnett, and W. A. Smith, Nat. Commun. **8**, 15968 (2017).
[66]S. A. Dayeh, D. Susac, K. L. Kavanagh, E. T. Yu, and D. Wang, Adv. Funct. Mater. **19**, 2102 (2009).
[67]K. Zhang, Y. Dai, Z. Zhou, S. U. Jan, L. Guo, and J. R. Gong, Nano Energy **41**, 101 (2017).
[68]S. Bednarek, B. Szafran, T. Chwiej, and J. Adamowski, Phys. Rev. B **68**, 045328 (2003).
[69]DLMF, NIST digital library of mathematical functions, http://dlmf.nist.gov/, Release 1.0.21 of 2018-12-15, edited by F. W. J. Olver, A. B. Olde Daalhuis, D. W. Lozier, B. I. Schneider, R. F. Boisvert, C. W. Clark, B. R. Miller, and B. V. Saunders (Eqs. 7.2.3 and 7.19.3), 2018.
[70]R. Kosloff and D. Kosloff, J. Comput. Phys. **63**, 363 (1986).
[71]D. Neuhauser and M. Baer, J. Chem. Phys. **90**, 4351 (1989).
[72]U. V. Riss and H.-D. Meyer, J. Phys. B: At., Mol. Opt. Phys. **26**, 4503 (1993).
[73]U. V. Riss and H.-D. Meyer, J. Chem. Phys. **105**, 1409 (1996).